Research Square

Preprints are preliminary reports that have not undergone peer review.
They should not be considered conclusive, used to inform clinical practice,
or referenced by the media as validated information.

In vivo measurement of light penetration in mouse and dog heads and human-head simulation for photocatalytic therapy in Alzheimer disease

Yuichi Kawai
The University of Tokyo
Mai Kuriyama
The University of Tokyo
Shinichi Torii
The University of Tokyo
James K Chambers
The University of Tokyo
Kazuyuki Uchida
The University of Tokyo
Youhei Sohma
Wakayama Medical University
Yuki Yamanashi
The University of Tokyo
Motomu Kanai
The University of Tokyo
Yukiko Hori
The University of Tokyo
Taisuke Tomita
taisuke@mol.f.u-tokyo.ac.jp

The University of Tokyo

Article

Keywords: biological window, optical penetration, phototherapy, Alzheimer disease, photo-oxygenation, Monte Carlo simulation

Posted Date: August 10th, 2026

DOI: https://doi.org/10.21203/rs.3.rs-10446700/v1

License: This work is licensed under a Creative Commons Attribution 4.0 International License.
Read Full License

Additional Declarations: Competing interest reported. YK is a full-time employee of USHIO Inc. The other authors declare that the research was conducted in the absence of any commercial or financial relationships that could be construed as a potential conflict of interest.

Version of Record: A version of this preprint was published at Scientific Reports on November 11th, 2026. See the published version at https://doi.org/10.1038/s41598-026-79461-7.

In vivo measurement of light penetration in mouse and dog heads and human-head simulation for photocatalytic therapy in Alzheimer disease.

Yuichi Kawai[1, 2*], Mai Kuriyama[1*], Shinichi Torii[1], James K Chambers[3], Kazuyuki Uchida[3], Youhei Sohma[4], Yuki Yamanashi[5], Motomu Kanai[5], Yukiko Hori[1†], Taisuke Tomita[1†]

[1] Laboratory of Neuropathology and Neuroscience, Graduate School of Pharmaceutical Sciences, The University of Tokyo, 7-3-1 Hongo, Bunkyo-ku, Tokyo 113-0033, Japan

[2] Ushio Inc. 6409 Moto-Ishikawa-cho, Aoba-ku, Yokohama-shi, Kanagawa, 225-0004, Japan

[3] Laboratory of Veterinary Pathology, Graduate School of Agricultural and Life Sciences, The University of Tokyo, 1-1-1 Yayoi, Bunkyo-ku, Tokyo, 113-8657, Japan.

[4] Department of Medicinal Chemistry, School of Pharmaceutical Sciences, Wakayama Medical University, Wakayama 640-8156, Japan

[5] Laboratory of Synthetic Organic Chemistry, Graduate School of Pharmaceutical Sciences, The University of Tokyo, 7-3-1 Hongo, Bunkyo-ku, Tokyo 113-0033, Japan

* These authors contributed equally to this work.

† Correspondence:

Yukiko Hori

yukiko-hori@mol.f.u-tokyo.ac.jp

Taisuke Tomita

taisuke@mol.f.u-tokyo.ac.jp

Abstract

Photoexcitation of chemical compounds, together with the light transmittance of the biological window, enables targeted phototherapy. We have developed a photocatalyst-based therapeutic approach for Alzheimer disease and demonstrated its efficacy in mice. However, it is unclear whether sufficient light energy can be delivered transcranially to target amyloid fibrils in the brains of larger animals, such as humans. Therefore, in this study, we measured the light energy from the body surface, through the skull, to the brain in mice and dogs. We then constructed an optical simulation model based on these measurements, and estimated the light energy reaching the brain from the human body surface. Our results show that only a small fraction of the light applied to the human body surface reaches the brain, with most energy loss occurring in the skin. In contrast, attenuation by the skull—the layer of greatest concern a priori—was relatively modest. These findings indicate that sufficient light energy can be delivered to the human brain *in vivo* through an appropriately designed delivery route and device, supporting the translational potential of photocatalytic therapy for Alzheimer disease.

Key words

biological window, optical penetration, phototherapy, Alzheimer disease, photo-oxygenation, Monte Carlo simulation

Introduction

The biological window refers to the orange-to-near-infrared (NIR) wavelength range in which light absorption is relatively low *in vivo*. It is used for measurements and imaging of deep tissues, as well as for phototherapy that relies on the excitation of endogenous chromophores and photosensitizing drugs *in vivo* [1, 2]. We have long focused on the tissue penetration of biological-window light and have been developing minimally invasive therapies for Alzheimer disease (AD) based on photocatalysis [3–5]. This approach uses a photocatalyst that specifically binds to amyloid-β (Aβ) fibrils, together with externally supplied light energy, to photo-oxygenate the Aβ fibrils, thereby promoting their degradation and clearance by immune cells. Previously, we demonstrated that Aβ fibrils accumulated in the brains of AD model mice, $App^{NL\text{-}G\text{-}F}$, could be cleared without surgery by irradiating the brain through the parietal scalp as the simplest and least invasive approach [5]. To bring this approach closer to clinical use, it is necessary to quantify the light energy reaching the animal brain and to determine how sufficient light energy can be delivered to human lesions.

Extensive studies have investigated optical penetration into living tissues, especially the brain, for applications including optogenetics, photobiomodulation, and NIR spectroscopy. These studies have reported many optical-penetration simulations using parameters such as the anisotropy factor, scattering coefficient, and absorption coefficient [6–8]. However, even with these prior studies, it remains difficult to determine the irradiation conditions under which our photocatalyst can effectively function in the human brain. One issue is how to validate the optical parameters used in the simulations. The optical behavior of biological tissues is known to be strongly affected by the physiological condition of the tissue sample [9, 10]. However, as described in [11], acquiring μ_s and μ_a for simulations typically requires excising the tissue, preparing and shaping the sample, and measuring it with a spectrophotometer, which makes it difficult to reproduce *in vivo* physiological conditions exactly. Another issue is that the excitation wavelength of our photocatalyst is shifted away from the 800–900 nm range that is frequently used in prior studies, because its molecular weight is designed to be relatively small to enhance blood–brain barrier permeability. As a result of this shift, optical parameters relevant to our wavelengths are relatively limited in the literature. Accordingly, the available parameters must be leveraged appropriately even when they derive from different species or sampling sites. These limitations are not unique to our approach and may arise more generally, potentially representing a bottleneck in the development of therapeutic agents and diagnostic modalities that rely on light energy.

The objective of this study is to predict optical penetration depth into the human brain by experimentally measuring penetrating light *in vivo* in mice and Beagle dogs on the short-wavelength side of the biological window (500–700 nm) and by using these measurements as a basis to evaluate and correct optical parameters for simulations of optical penetration depth in a human head model.

For the animal models, we used mice, which are commonly employed in experiments for *in vivo* evaluation across a wide range of diseases, and Beagle dogs, which are larger and have thicker skulls.

Materials & Methods

Irradiation light source

In this study, we used the same irradiation system as described previously [12]. The system comprised orange LEDs (Nichia Corporation) mounted on a circuit board, together with a light guide to homogenize the irradiance and generate a uniform light source. The irradiated area was 50 mm × 50 mm. Spectral measurements (USR-45, Ushio, Inc.) showed a center wavelength of 610 nm and a full width at half maximum (FWHM) of 86 nm, confirming that the system provided a broad spectrum covering the 500–750 nm range (Figure 1A).

Measurement device for tissue-transmitted light intensity

Measurements were performed using a needle-shaped probe equipped with a detector window and a light guide, together with a spectrophotometer (FLAME-T, Ocean Optics, Inc.). The probe was a hollow metal tube, and we used probes with different inner diameters for mice and dogs (mouse: 0.8 mm, dog: 4.0 mm). The probe had a sharply machined tip and a detector window on the side. Light entering through the detector window was guided to the spectrophotometer via the light guide inside the probe, and the resulting spectral irradiance was measured (Figure 1B).

The penetration of incident light into biological tissue was evaluated by comparing the intensity of the same wavelength component λ between two positions: the receiving intensity $I(\lambda)$ at a predetermined location within the tissue and the receiving intensity $I_0(\lambda)$ when the detector window was placed directly beneath the irradiation surface of the light source. The tissue spectral transmittance $T(\lambda)$ was then calculated as:

$$T(\lambda) = \frac{I(\lambda)}{I_0(\lambda)} \dots \text{Eq.1}$$

Animals

We used 8-week-old male C57BL/6JmsSlc mice (Japan SLC, Inc.), weighing 21.7 ± 1.2 g (n = 7). We also used Beagle dog specimens obtained from NAS Laboratory, Ltd. within 1 h after

euthanasia. The dogs were 15–24 months old, female, and weighed 10.2 ± 1.1 kg (n = 3). All mouse experiments, including euthanasia, were conducted in accordance with the guidelines of the Institutional Animal Care Committee of the Graduate School of Pharmaceutical Sciences, University of Tokyo. This experimental study received approval from the Institutional Ethics Committee of the Graduate School of Pharmaceutical Sciences, University of Tokyo as protocol number P5-10. Anesthesia was induced by first exposing the animals to isoflurane vapor in an enclosed chamber, followed by intraperitoneal injection of a three-drug mixture (midazolam, medetomidine, and butorphanol) with a volume of 50 μL per 10 g of body weight. After the experiment was completed, the mice were euthanized by creating a hole in the diaphragm under anesthesia. For the dog experiments, no live animal procedures were performed by the authors. The dog tissues used in this work were obtained as post-mortem by-products from animals euthanized for other purposes at NAS Laboratory, Ltd., in accordance with NAS Laboratory's institutional procedures. For those animals, prior to euthanasia, anesthesia was induced by intramuscular administration of xylazine (2 mg/kg) and ketamine hydrochloride (15 mg/kg); euthanasia was performed by exsanguination via bleeding from the carotid artery.

Spectral transmittance of mouse tissue

The manipulation of the probe detector window was performed using a stereotaxic apparatus (#68030, RWD Life Science) and an X–Y–Z-axis mechanical stage (Chuo Seiki Co., Ltd.). Using the brain coordinate system relative to bregma reported by Paxinos and Franklin [13], the coordinates of the detector window were aligned with the hippocampus (ML +1.5 mm, AP -2.0 mm, DV -1.7 mm). After anesthetizing the mice, the temporal region was incised, and a small craniotomy was created with a mini-rotary tool (#28511, PROXXON). The probe was then slowly inserted along the mediolateral direction through the opening (Figure 2A). After probe insertion, the irradiation light source was switched on, and the spectral irradiance of the light incident on the spectrophotometer was recorded. The tissue spectral transmittance was obtained by calculating the ratio of the measured spectral irradiance to the corresponding baseline value.

Spectral transmittance of Beagle dog tissue

In the dog experiments, the probe was manually manipulated. To align the probe's detector window with the hippocampus, preliminary experiments were conducted, and the insertion location and depth were determined in advance. Following euthanasia, as shown in Figure 3A, the temporal muscle was incised at its center to split it and expose the skull. A burr hole was then made at the center

of the surgical field using an electric drill, aligned along the mediolateral direction for probe insertion. The probe was advanced from the detector window along the mediolateral axis until the segment 3 cm from the window reached the skull surface, positioning the detector window in the vicinity of the hippocampus.

Thereafter, the irradiation light source was pressed against the parietal scalp and switched on. The spectral irradiance of the light incident on the spectrophotometer was recorded, and the tissue spectral transmittance from the parietal scalp surface to the hippocampus was obtained by calculating the ratio to the corresponding baseline value. Similarly, the spectral transmittance from the parietal scalp surface to the inner surface of the parietal scalp and from the inner surface of the parietal scalp to the inner surface of the skull were obtained sequentially from the same Beagle dog. After extracting the brain, the spectral transmittance from the brain surface to the hippocampus was obtained (Figure 3B). The region from the parietal scalp surface to the inner surface of the parietal scalp was defined as the skin layer, the region from the inner surface of the parietal scalp to the inner surface of the skull as the skull layer, and the region from the brain surface to the vicinity of the hippocampus as the brain layer, corresponding to the optical model described below.

Simulation

Monte Carlo simulations were performed using Advanced Systems Analysis Program 2023 V1 SP3 (BREAULT RESEARCH ORGANIZATION, INC.). The tissues from the outside of the body to the hippocampus were simplified into three elements—the skin layer, the skull layer, and the brain layer—and modeled as planar scattering media arranged in a layered configuration. The simulation model consisted of a Lambertian planar light source, a detector, and layered scattering-medium models corresponding to each tissue layer located between them (Figures 4, 5A, and 6A). The simulated transmitted light intensity, $T_{simu}(\lambda)$, was calculated as the ratio between the optical flux incident on the central region of the top surface of the scattering-medium model and the optical flux collected by the detector from the scattering-medium model exiting from the central region of the bottom surface (as in Eq. 1). The number of photons was set to 1,000,000 for the calculations in Figures 4 and 5C, and 10,000,000 for the calculations in Figures 5B and 6.

Simulation parameters

The scattering-medium model was parameterized using the scattering coefficient μ_s and the absorption coefficient μ_a as the dominant optical parameters to represent each tissue layer. When wavelength-dependent sets of these parameters were available in the software toolkit, they were used

as the initial values; otherwise, values cited from the literature were adopted. The thickness of the layered scattering-medium model was set to the mean value measured with a caliper or by image analysis when actual tissue samples corresponding to the *in vivo* measurement were obtainable; otherwise, literature-reported values or values cited from the software toolkit were used. The parameter values used and their sources are summarized in Table 1.

Modification of optical parameters

Using a fitting parameter p, the scattering coefficient or absorption coefficient (collectively denoted as $\mu(\lambda)$) was modified linearly using one of the following approaches, and the simulated spectral transmittance $T_{simu}(\lambda)$ for each tissue was fitted to the measured transmittance $T_{measured}(\lambda)$.

(i) Scaling: correction for a uniform difference in the concentration of absorbers and scatterers

$$\mu_{mod}(\lambda) = p\mu(\lambda) \quad \ldots \text{Eq. 2}$$

(ii) Mixing (interpolation): coexistence of two tissue components $\mu_1(\lambda)$ and $\mu_2(\lambda)$

$$\mu_{mod}(\lambda) = p\mu_1(\lambda) + (1-p)\mu_2(\lambda) \quad \ldots \text{Eq. 3}$$

(iii) Addition: addition of a chromophore component $\mu_2(\lambda)$ to a tissue component $\mu_1(\lambda)$

$$\mu_{mod}(\lambda) = \mu_1(\lambda) + p\mu_2(\lambda) \quad \ldots \text{Eq. 4}$$

Since $T(\lambda)$ spans several orders of magnitude (from 10^{-2} to 10^{-10}), the contribution from regions with small transmittance would be underestimated in the residual sum of squares if the transmittance itself were used directly. Therefore, the common logarithm of $T(\lambda)$ was used to compute the residual sum of squares RSS:

$$RSS = \sum_{\lambda}(\log_{10} T_{simu}(\lambda) - \log_{10} T_{measured}(\lambda))^2 \quad \ldots \text{Eq. 5}$$

To compare $T_{simu}(\lambda)$ with the measured transmittance $T_{measured}(\lambda)$ and the error bar $SD_{measured}(\lambda)$ of the measured data, the absolute residual $R(\lambda)$ was used:

$$R_{simu}(\lambda) = |\log_{10} T_{simu}(\lambda) - \log_{10} T_{measured}(\lambda)| \quad \ldots \text{Eq. 6}$$

$$R_{measured}(\lambda) = |\log_{10}(T_{measured}(\lambda) + SD_{measured}(\lambda)) - \log_{10} T_{measured}(\lambda)| \quad \ldots \text{Eq. 7}$$

If $R_{simu}(\lambda) < R_{measured}(\lambda)$, the fitted model was interpreted as adequately representing the measured values in that wavelength region.

Statistical analysis

The measured values of transmitted light through tissue were obtained by performing multiple measurements for each individual animal ($n \geq 3$). The representative value was defined as the mean obtained by averaging the individual-wise mean values across animals. The sample standard deviation was calculated from the variability of the individual-wise mean values obtained from the multiple measurements. In the text, the results are presented as the representative value ± the sample standard deviation. In the figures, the representative value is shown by a circle (○), and the sample standard deviation is shown as error bars.

Data Availability

The datasets generated and/or analysed during the current study are not publicly available due to contractual restrictions and licensing terms that prohibit public redistribution but are available from the corresponding author on reasonable request.

Results

In vivo *measurement of tissue spectral transmittance*

To obtain the experimental values for comparison with the simulations, we first measured the spectral transmittance $T_{measured}(\lambda)$ in each tissue of mice and dogs. For mice, because the body size was very small, we measured only the spectral transmittance from the parietal scalp surface to the vicinity of the hippocampus (Figure 2B). Additionally, we confirmed that the heart continued to beat until the time of dissection used to verify the position of the detector window. For dogs, because the body size was sufficiently large, in addition to the spectral transmittance from the parietal scalp surface to the vicinity of the hippocampus, we also measured the spectral transmittance corresponding to the following regions: from the parietal scalp surface to the inner surface of the parietal scalp, from the inner surface of the parietal scalp to the inner surface of the skull, and from the parietal brain surface to the vicinity of the hippocampus (corresponding to the skin layer, skull layer, and brain layer, respectively) (Figure 3C). We also confirmed by dissection that the probe track passed near the hippocampus, with no marked bleeding. In both groups, the spectral transmittance exhibited a rapid change over the 580–620 nm range. In particular, for dog brain tissues with a longer optical path length, the transmittance fell below 10^{-4}, resulting in substantial noise and missing measurements due to insufficient received light intensity. In contrast, the measurement variability (standard deviation) was generally within 0.3 log and at most within 0.5 log, indicating that inter-individual variability was not large.

Modification of optical parameters for this study

We next modified the reference optical parameter values shown in Table 1 using Eqs. 2–4, based on the measured tissue spectral transmittance $T_{measured}(\lambda)$ obtained in Figures 2 and 3. First, for the skin layer (Figure 4A), the initial simulation transmittance $T_{simu}(\lambda)$ was overestimated relative to $T_{measured}(\lambda)$. Therefore, we performed a fitting procedure by scaling the scattering coefficient μ_s using Eq. 2. As a result, we achieved $R_{simu}(\lambda) < R_{measured}(\lambda)$ in all wavelength ranges included in the simulation. Next, for the skull layer (Figure 4B), the initial simulation transmittance $T_{simu}(\lambda)$ was underestimated relative to $T_{measured}(\lambda)$. Therefore, we performed a fitting procedure by scaling both the scattering coefficient μ_s and the absorption coefficient μ_a using Eq. 2. As a result, $R_{simu}(\lambda) < R_{measured}(\lambda)$ could be achieved in most of the wavelength ranges included in the simulation (510–660 nm). Finally, for the brain layer (Figure 4C), the measured spectral transmittance $T_{measured}(\lambda)$ was bracketed by the spectral transmittance $T_{simu}(\lambda)$ calculated from literature values for white matter and gray matter. However, the rapid transmittance change over the 580–620 nm range—presumably due to the influence of hemoglobin—was not

reproduced in $T_{simu}(\lambda)$. Therefore, we first optimized the scattering and absorption coefficients (μ_s and μ_a) of white matter and gray matter by interpolation (mixing) using Eq. 3 in the 680–700 nm range, where hemoglobin absorption is minimal. Subsequently, for 580 nm, we added the hemoglobin absorption coefficient at its absorption maximum using Eq. 4, which enabled us to obtain $R_{simu}(\lambda) < R_{measured}(\lambda)$ at 580 nm and in the 660–700 nm range.

Validation of the modified results

Next, we compared the simulated spectral transmittance values $T_{simu}(\lambda)$, including all tissue-layer elements, with the measured values $T_{measured}(\lambda)$, and evaluated the validity of the optical parameters optimized for each layer in Figure 4. First, Figure 5B shows the comparison between $T_{simu}(\lambda)$ and $T_{measured}(\lambda)$ for the spectral transmittance from the dog parietal scalp surface to the vicinity of the hippocampus. As shown in Figure 3C, $T_{measured}(\lambda)$ from the dog parietal scalp surface to the vicinity of the hippocampus was less than 10^{-4} in most wavelength regions. In particular, on the short-wavelength side, the measurements were difficult due to insufficient signal intensity. Therefore, the wavelength range in which a meaningful comparison with the simulation was possible was limited to 650–700 nm. However, in most regions, $R_{simu}(\lambda) > R_{measured}(\lambda)$, indicating that $T_{simu}(\lambda)$ was underestimated by approximately 0.7–0.9 log relative to $T_{measured}(\lambda)$. Next, Figure 5C shows the comparison between $T_{simu}(\lambda)$ and $T_{measured}(\lambda)$ for the spectral transmittance from the mouse parietal scalp surface to the vicinity of the hippocampus. As in the dog case, in the 610–700 nm range that was not affected by hemoglobin, $R_{simu}(\lambda) > R_{measured}(\lambda)$, and $T_{simu}(\lambda)$ was underestimated by approximately 0.2–0.3 log relative to $T_{measured}(\lambda)$. For wavelengths below 600 nm, $T_{simu}(\lambda)$ was overestimated relative to $T_{measured}(\lambda)$, with a magnitude slightly larger than that in the 610–700 nm range, corresponding to 0.3–0.5 log. This discrepancy was reduced by modifying the model using the addition of the hemoglobin absorption coefficient (Eq. 4). As a result, in the 510–620 nm range, we achieved $R_{simu}(\lambda) < R_{measured}(\lambda)$. However, even after this modification, in the 630–700 nm range we still obtained $R_{simu}(\lambda) > R_{measured}(\lambda)$.

Simulation of deep-penetrating light in the human brain

Finally, in a three-layer model scaled up to the human case, we performed simulations of optical penetration from the body surface toward the brain using the parameters optimized in Figure 5C. The relationship between the penetration depth from the parietal scalp surface and the transmitted light intensity $T_{simu}(\lambda)$ is shown in Figure 6B. The optical energy that penetrates the skull and reaches the brain surface was markedly larger on the longer-wavelength side, with 600 nm serving as

an apparent boundary, as also suggested by the above penetration behavior (Figure 2B, 3C). For instance, at 620 nm, it was estimated that 10^{-7} of the incident light reached the brain surface, whereas at 680 nm (the longer-wavelength side), 10^{-6} of the incident light reached the brain surface.

In the simulation, the light irradiated from the parietal scalp surface was strongly attenuated in the skin tissue, mainly because the human skin layer is approximately three times as thick as that of the dog (Table 1). In particular, for wavelengths below 580 nm, where the influence of hemoglobin is substantial, the light was estimated to attenuate to the order of 10^{-7}. This attenuation became weaker as the wavelength increased, and it was reduced to the order of 10^{-4} in the wavelength range of 650 nm and above. In deeper layers including skull and brain, the attenuation was relatively gradual. For example, in the wavelength range below 580 nm, the penetration depth at which the intensity decreases to 10^{-1} of its value was estimated to be approximately 0.45 mm in the skin layer, whereas it was approximately 2.0 mm in the skull layer. Moreover, in the longer-wavelength range of 650 nm and above, the spacing between successive 10-fold attenuation contours increased: in each layer, the penetration depth for 10^{-1} attenuation was estimated to be approximately 1.5 mm in the skin layer, while it was approximately 5.5 mm in the skull and brain layers.

Discussion

In this study, we measured how much light reaches the brain from the body surface in animals—mice under anesthesia and dogs immediately after death. Using optical parameters consistent with these measurements, we then simulated light penetration in a human head model to estimate how much light could reach the brain from the body surface in living humans. These results enable us to predict the light energy required for AD therapy by photo-oxygenation of amyloid fibrils, and provide a basis for discussing both the devices needed to deliver this energy and the photocatalyst performance needed for sufficient therapeutic efficacy.

In the *in vivo* measurement of penetrating light, we measured the light energy reaching the vicinity of the hippocampus under near-physiological conditions using the light-guide probe, with a reproducibility of approximately ±0.3 log. The dissection to verify the position of the detector window confirmed that the measured distance from the brain surface to the detector window was 1.8 ± 0.13 mm, which was close to the hippocampal coordinate (DV −1.7 mm) in the atlas by Paxinos and Franklin. Thus, Figure 2B can be used both to refine the optical parameters for the simulations and to estimate the light energy delivered to the hippocampus in our previous mouse experiments under the same irradiation conditions. In the dogs as well, there were no apparent obstacles to probe access to the tissue and no noticeable tissue disruption. As with the mice, these results should be useful for estimating the light energy reaching the target tissue in animal experiments.

In the optical penetration-depth simulations, we used the tissue layer–specific spectral transmittance obtained from *in vivo* measurements in dogs. By proportionally fitting the literature optical parameters to these values, we obtained simulations that closely matched the measurements (Figure 4). When the modified parameters were applied to mice—whose data were not used for the fitting— the calculated transmittance still agreed with the *in vivo* measurements (Figure 5). We therefore considered that these parameters are valid across different species and length scales, and ultimately used them to predict the spectral transmittance between the human body surface and the brain (Figure 6).

Nevertheless, our approach has three difficult-to-avoid limitations in predicting how much light energy penetrates into the human body. The first limitation is the invasiveness of the probe. Probe insertion inevitably damages tissue, and the difficulty of accessing deep regions prolongs the measurement, driving the tissue away from its physiological state. A thinner probe and a smaller incision would reduce this damage; however, such probes are more fragile and more difficult to handle. The second limitation is the impact of anesthesia and euthanasia. Fixing the probe and the irradiation light source requires anesthesia or euthanasia, both of which alter blood flow and oxygen saturation. For example, the marked increase in $R_{simu}(\lambda)$ around 600 nm in Figure 4C probably reflects a spectral shift arising from differences in hemoglobin oxygen saturation between the literature parameter values and our *in vivo* measurements. Similarly, the underestimation of hemoglobin absorption (~600 nm) in the simulation shown in Figure 5C likely reflects differences in tissue blood volume between dogs after euthanasia and mice under anesthesia. The third limitation is limited experimental data. There are two optical phenomena that contribute to light penetration in living tissue: (i) scattering from the tissue surface and (ii) absorption within the tissue. However, because our photometric probe measures only transmittance, these two cannot be separated, and proportional corrections are applied to both the scattering and absorption coefficients. When tissue is detached from the living body, structural changes readily increase scattering in the superficial region. In our correction, such scattering-related changes are attributed to both coefficients, leading to overestimation of the absorption coefficient. This effect grows with tissue thickness; thus, in thick-tissue simulations such as Figure 5B, $T_{simu}(\lambda)$ would be expected to be underestimated. Because the human model is the thickest, the transmittance shown in Figure 6 can also be considered to be underestimated overall.

This work also highlights the practical use of light to deliver energy within living tissue. As shown in Figure 6, 500–600 nm light barely reaches the brain surface, whereas at 650–700 nm (and above), on the order of 10^{-6} of the incident light reaches it. At a realistic phototherapy irradiance of 10^{-1} W/cm2, this corresponds to about 3.6×10^{-4} J/cm^2 reaching the brain surface per hour. For light penetration into the hippocampus, since the optical path from the brain surface to the hippocampus is 35 mm [20] even via the shortest route, irradiation from the body surface must overcome an attenuation

of approximately 10^{-12}–10^{-13}. However, Figure 6 also showed that most attenuation occurs within the ~4.9-mm-thick skin tissue, with comparatively little in the skull and brain. Although invasiveness would increase, this suggests that much more light could be delivered into the brain by bypassing the skin. For example, skull transmission attenuates the light to approximately 10^{-2} at 650 nm. Given the photocatalyst sensitivity we previously reported (ED_{50} = 6.05 J/cm^2 [12]), and considering that our simulations likely underestimate the delivered light energy, we can estimate that about 2 hours or less of irradiation from the skull surface could deliver to the brain surface light energy comparable to the ED_{50} of photo-oxygenation. This would enable photo-oxygenation within the several millimeters of the brain. Therefore, with an appropriately designed delivery route and device, photo-oxygenation could become a viable AD therapy.

Conclusion

In this study, we showed that brain-penetrating light on the short-wavelength side of the biological window can be estimated across animal species by combining literature absorption and scattering coefficients with a simple *in vivo*-based modification. Moreover, the resulting human-tissue simulation model enables us to specify concrete requirements for photo-oxygenation in AD therapy and provides insight into light-delivery routes that minimize optical energy losses.

References

[1] Anderson, R. R. & Parrish, J. A. The optics of human skin. *J. Invest. Dermatol.* **77**, 13–19 (1981).

[2] Hong, G., Antaris, A. & Dai, H. Near-infrared fluorophores for biomedical imaging. *Nat. Biomed. Eng.* **1**, 0010 (2017).

[3] Ni, J. et al. Near-infrared photoactivatable oxygenation catalysts of amyloid peptide. *Chem* **4**, 807–820 (2018).

[4] Ozawa, S. et al. Photo-oxygenation by a biocompatible catalyst reduces amyloid-β levels in Alzheimer's disease mice. *Brain* **144**, 1884–1897 (2021).

[5] Nagashima, N. et al. Catalytic photooxygenation degrades brain Aβ *in vivo*. *Sci. Adv.* **7**, eabc9750 (2021).

[6] Yue, L. & Humayun, M. S. Monte Carlo analysis of the enhanced transcranial penetration using distributed near-infrared emitter array. *J. Biomed. Opt.* **20**, 088001 (2015).

[7] Pitzschke, A. et al. Red and NIR light dosimetry in the human deep brain. *Phys. Med. Biol.* **60**, 2921–2937 (2015).

[8] Li, T., Xue, C., Wang, P., Li, Y. & Wu, L. Photon penetration depth in human brain for light stimulation and treatment: a realistic Monte Carlo simulation study. *J. Innov. Opt. Health Sci.* **10**, 1743002 (2017).

[9] Hamdy, O., Abdel-Salam, Z. & Abdel-Harith, M. Optical characterization of biological tissues based on fluorescence, absorption, and scattering properties. *Diagnostics* **12**, 2846 (2022).

[10] Jacques, S. L. Optical properties of biological tissues: a review. *Phys. Med. Biol.* **58**, R37–R61 (2013).

[11] Awazu, K. Measurement and calculation of optical properties for biological tissues. *Jpn. J. Opt.* **41**, 444–449 (2012).

[12] Kawai, Y. et al. The dynamics of oxygenation to Aβ fibrils using an azobenzene-boron complex type photocatalyst and light energy. *Sci. Rep.* **15**, 25241 (2025).

[13] Paxinos, G. & Franklin, K. B. J. *The Mouse Brain in Stereotaxic Coordinates, Compact* 3rd edn (Academic Press, 2008).

[14] Jung, E. C. & Maibach, H. I. Animal models for percutaneous absorption. *J. Appl. Toxicol.* **35**, 1–10 (2015).

[15] Lapchak, P. A. et al. Transcranial near-infrared laser transmission (NILT) profiles (800 nm): systematic comparison in four common research species. *PLoS One* **10**, e0127580 (2015).

[16] Ekşi, M. Ş., Güdük, M. & Usseli, M. I. Frontal bone is thicker in women and frontal sinus is larger in men: a morphometric analysis. *J. Craniofac. Surg.* **32**, 1683–1684 (2021).

[17] Haleh, S., Hirac, G. & Frédéric, P. Optical properties of mice skull bone in the 455- to 705-nm range. *J. Biomed. Opt.* **22**, 010503 (2017).

[18] Yaroslavsky, A. N. et al. Optical properties of selected native and coagulated human brain tissues *in vitro* in the visible and near infrared spectral range. *Phys. Med. Biol.* **47**, 2059–2073 (2002).

[19] Bosschaart, N., Edelman, G. J., Aalders, M. C., van Leeuwen, T. G. & Faber, D. J. A literature review and novel theoretical approach on the optical properties of whole blood. *Lasers Med. Sci.* **29**, 453–479 (2014).

[20] Bellier, A. et al. Micro to macro scale anatomical analysis of the human hippocampal arteries with synchrotron hierarchical phase-contrast tomography. *Surg. Radiol. Anat.* **46**, 1753–1760 (2024).

Funding

This work was supported in part by a Grant-in-Aid for Scientific Research (C) (JP18K06653 to Y.H.), a Grant-in-Aid for Challenging Exploratory Research (JP19K22484 to Y.S.), a Grant-in-Aid for Scientific Research (B) (JP23K21357, JP25K02405 to Y.H. and JP24K02153 to Y.S.), a Grant-in-Aid for Scientific Research (A) (JP23H00394 to T.T.), a Grant-in-Aid for Scientific Research (S) (JP23H05466 to M.K.), a Grant-in-Aid for Early-Career Scientists (JP26K18439 to Y.Y.), Grant-in-Aid for Transformative Research Areas (B) (JP23H05036 to Y.H.) from the Japan Society for the Promotion of Science (JSPS), grants from Innovative Research Group by the Strategic International Brain Science Research Promotion Program (Brain/MINDS Beyond) (JP19dm0307030 to Y.H.), AMED-PRIME (JP24gm6410017 to Y.H.), Practical Research Project for Rare/Intractable Diseases (JP25ek0109834 to Y.H.), Brain Mapping by Integrated Neurotechnologies for Disease Studies (Brain/MINDS) (JP22dm0207072 to T.T.), Research and Development Grants for Dementia (21dk0207046, 23dk0207061 and 24dk0207073 to T.T.) and Strategic International Collaborative Research Program (SICORP) (JP19jm0210058 to Y.S.) from the Japan Agency for Medical Research and Development (AMED), a Joint research funds with USHIO Inc..

Author Contributions

YK and MKu performed experiments. YK wrote the draft and revised it. ST, JKC, KU, YS, YY, MKa, YH and TT were involved in discussing, drafting, and editing the manuscript. All authors approved the submitted version.

Conflict of Interest

YK is a full-time employee of USHIO Inc. The other authors declare that the research was conducted in the absence of any commercial or financial relationships that could be construed as a potential conflict of interest.

Acknowledgements

We would like to thank Tomohiko Kio, Hiroshi Shibata (Ushio Inc.), Takashi Kaneda (NAS Laboratory Inc.) for technical assistance.

Table

Table 1. List of the tissue thicknesses and optical parameters used in the 3-layer simulations.

Parameters that could be measured experimentally in *in vivo* transmittance measurements are marked with an asterisk (*). Parameters that were provided within the simulation software are marked with a double asterisk (**). For all other parameters, values were cited from the literature (with the corresponding reference numbers indicated).

***Because an accurate simulation of a long optical path length is difficult, the simulations were performed for an optical path length of 20.0 mm.

Tissue	Thicknesses of the simulation layers *d* [mm]			optical parameters
	Mouse	Dog	Human	
Skin layer	0.80 [14]	1.5* (n=1)	4.9**	ASAP internal parameters **
Skull layer	0.44 [15]	5.5* (n=1)	10.0 [16]	Ref. [17]
Brain layer	1.8±0.13* (n=5)	13±2.5* (n=3)	20.0***	Ref. [18]
Whole blood	–	–	–	Ref. [19]

Figure legends

Figure 1. Instrumentation used for in vivo *measurement of tissue-transmitted light.*

(A) Appearance and spectrum of the light source used for irradiation. Orange LEDs were arranged in a planar array and homogenized using a light guide to form a uniform light source, providing a broad spectrum across 500–750 nm. (B) A needle-shaped probe. It has a handle and a light guide that delivers light entering through the detector window to the spectrophotometer.

Figure 2. Measurement of spectral transmittance from the parietal scalp surface to the hippocampus in mice.

(A) Instrumentation used for the measurements. The mice were immobilized in a custom-built stereotaxic apparatus that enabled the coordinates of the probe detector window to be manually adjusted with a micrometer, allowing vertical irradiation from the parietal scalp surface. (B) Results of spectral transmittance measurements. From the spectral transmittance curves (———), data were extracted at every 10 nm, plotted as markers (○), and error bars were added. Error bars: standard deviation.

Figure 3. Measurement of tissue spectral transmittance in dogs.

(A) Access of the optical probe to the vicinity of the hippocampus. The temporalis muscle was incised at the indicated location to expose the skull, and the optical probe was then inserted through a hole made in the skull. (B) Anatomical relationships of the measurement sites in tissue-wise transmittance measurements. (C) Results of tissue-wise spectral transmittance measurements. The mean spectral transmittance values obtained from multiple measurements are shown by the line (———). Data were extracted at every 10 nm and plotted as markers to indicate the measurement sites: ○, parietal scalp surface to the vicinity of the hippocampus; △, parietal scalp surface to the inner surface of the parietal scalp (skin layer); □, inner surface of the parietal scalp to the inner surface of the skull (skull layer); ◇, parietal brain surface to the vicinity of the hippocampus (brain layer). Error bars: standard deviation.

Figure 4. Fitting of tissue-wise optical models to in vivo transmittance measurements in dogs.

For each tissue layer—(A) the skin layer, (B) the skull layer, and (C) the brain layer—we show (top) the graph of the fitting results and (bottom) a schematic of the fitted optical model. The legend for the plots is as follows: ○: tissue spectral transmittance $T_{measured}(\lambda)$ sampled every 10 nm; -------:

initial simulation value $T_{simu}(\lambda)$; ———: optimized simulation value $T_{simu}(\lambda)$; ------: $R_{simu}(\lambda)$; ———: $R_{measured}(\lambda)$. Error bars: standard deviation. The schematic shows the optical rays emitted from a planar light source above the tissue model, the individual tissue layers, and the detector position.

Figure 5. Comparison between the optimized optical model and in vivo *transmittance measurements.* (A) Schematic of the optical model used for the simulation. (B) Comparison with *in vivo* transmittance measurements in dogs (parietal scalp surface to the vicinity of the hippocampus). (C) Comparison with *in vivo* transmittance measurements in mice (parietal scalp surface to the vicinity of the hippocampus). The legend for the plots is as follows: ○: tissue spectral transmittance $T_{measured}(\lambda)$ extracted at every 10 nm; ------: $R_{simu}(\lambda)$; ———: $R_{measured}(\lambda)$. Error bars: standard deviation. For (B), ———: simulated $T_{simu}(\lambda)$ using the parameters obtained in Figure 4. For (C), -------: simulated $T_{simu}(\lambda)$ using the parameters obtained in Figure 4; ———: simulated $T_{simu}(\lambda)$ using the parameters obtained in Figure 4 with additional hemoglobin absorption.

Figure 6. Light-penetration simulation results in human head tissue.

(A) Schematic of the optical model used for the simulation. (B) Simulation results. The legend is as follows: ------: tissue boundaries in the 3-layer model. The boundaries near 5 mm correspond to the interface between the skin and the skull, and those near 15 mm correspond to the interface between the skull and the brain. ——— or ———: depth (as a function of wavelength) at which light with an intensity reduced to 10^{-1} to 10^{-10} of the incident light can reach. ———corresponds to 10^{-5} and 10^{-10}, while ———corresponds to the other intensity levels.

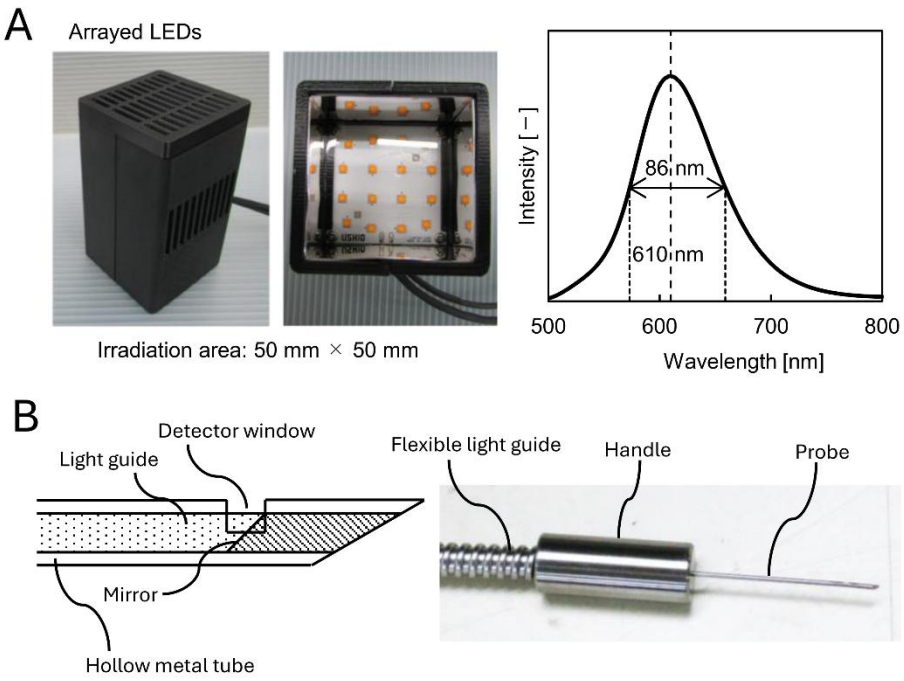

A
Arrayed LEDs
Irradiation area: 50 mm × 50 mm
Intensity [−]
86 nm
610 nm
500
600
700
800
Wavelength [nm]
B
Detector window
Light guide
Mirror
Hollow metal tube
Flexible light guide
Handle
Probe

Figure 1

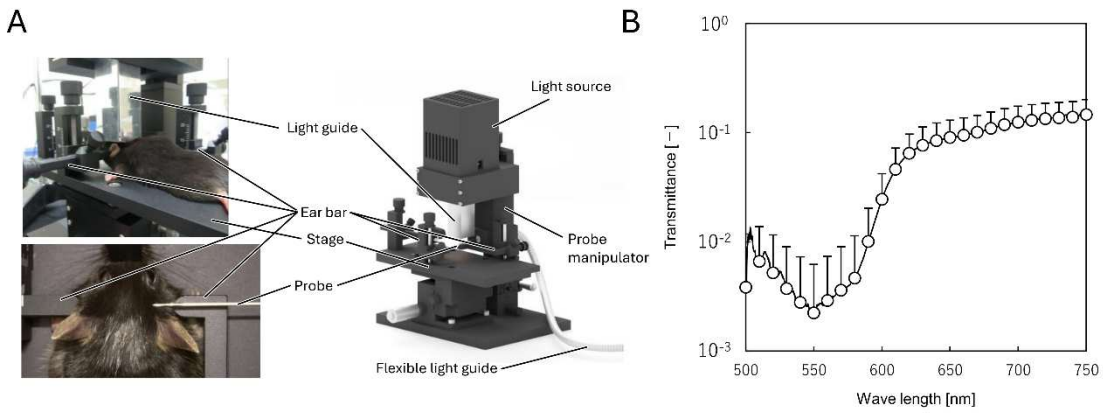

A
Light guide
Ear bar
Stage
Probe
Light source
Probe manipulator
Flexible light guide
B
Transmittance [−]
10^{0}
10^{-1}
10^{-2}
10^{-3}
500
550
600
650
700
750
Wave length [nm]

Figure 2

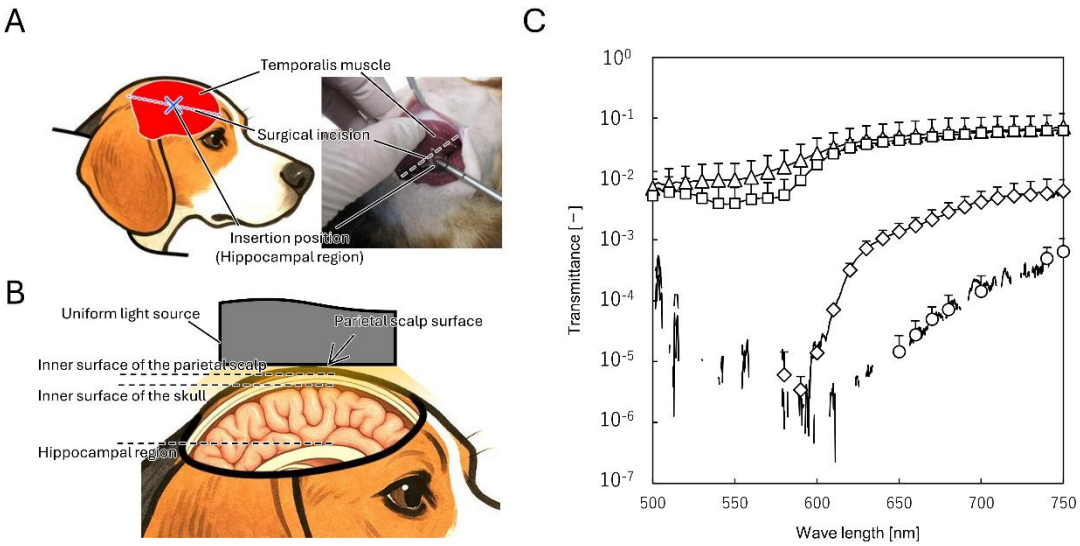
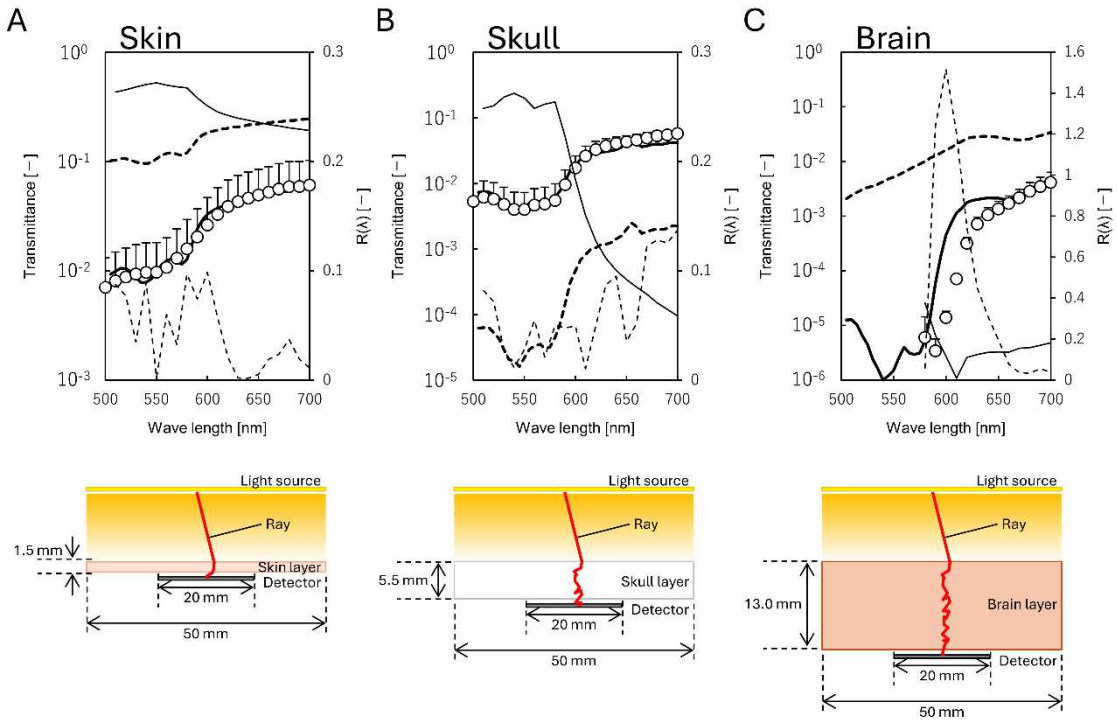

A
Temporalis muscle
Surgical incision
Insertion position
(Hippocampal region)
B
Uniform light source
Parietal scalp surface
Inner surface of the parietal scalp
Inner surface of the skull
Hippocampal region
C
Transmittance [−]
10^{0}
10^{-1}
10^{-2}
10^{-3}
10^{-4}
10^{-5}
10^{-6}
10^{-7}
500
550
600
650
700
750
Wave length [nm]

Figure 3



552

553

554

555

556

557 Figure 4

558

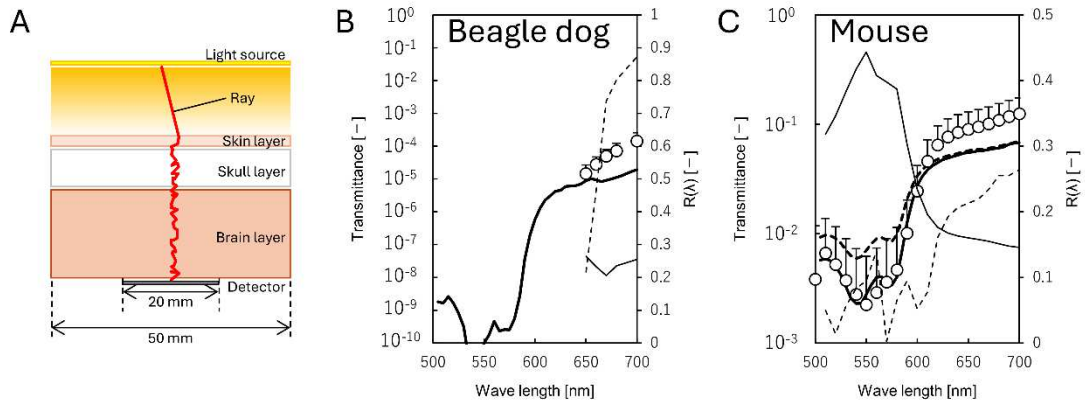

A
Light source
Ray
Skin layer
Skull layer
Brain layer
Detector
20 mm
50 mm
B
Beagle dog
Transmittance [−]
R(λ) [−]
Wave length [nm]
C
Mouse
Transmittance [−]
R(λ) [−]
Wave length [nm]

Figure 5

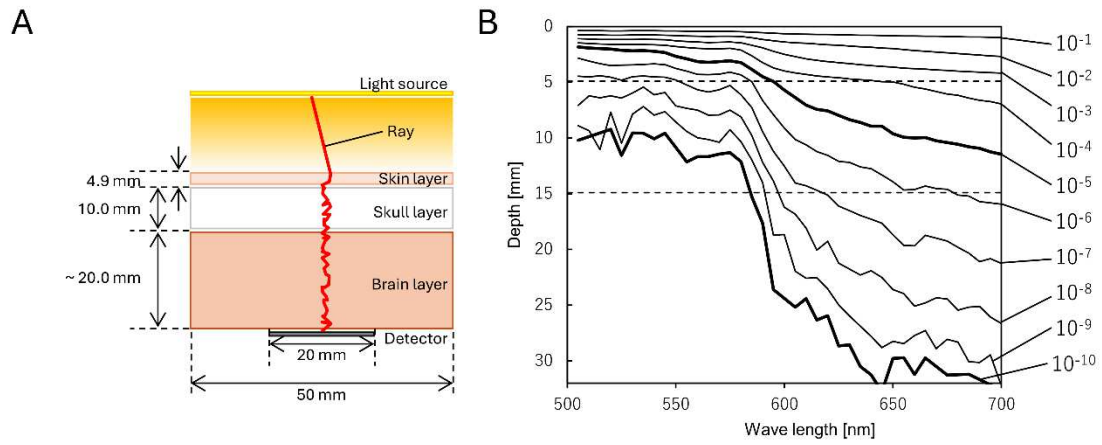

A
Light source
Ray
Skin layer
Skull layer
Brain layer
Detector
4.9 mm
10.0 mm
~ 20.0 mm
20 mm
50 mm
B
Depth [mm]
Wave length [nm]
0
5
10
15
20
25
30
500
550
600
650
700
10-1
10-2
10-3
10-4
10-5
10-6
10-7
10-8
10-9
10-10

Figure 6